Carbon Reports
Vol. 5 No. 1 2026 **40-47**

Research Paper

The structural stability and capacity increase of a phosphorus-doped hard carbon produced by zinc oxide templating used in sodium-ion batteries:

Hideka Ando[a),*], Yasuhiro Toyoda[b)], Kenya Fujino[b)], Kenjiro Hashi[a)], Shinobu Ohki[a)], Yuki Fujii[c)], Daisuke Igarashi[c)], Shinichi Komaba[c)] and Kazuma Gotoh[b)]

a) National Institute for Materials Science: 3–13 Sakura, Tsukuba, Ibaraki 305–0003, Japan
b) Center for Nano Materials and Technology, Japan Advanced Institute of Science and Technology: 1–1 Asahidai, Nomi, Ishikawa 923–1292, Japan
c) Department of Applied Chemistry, Tokyo University of Science: 1–3 Kagurazaka, Shinjuku-ku, Tokyo 162–8601, Japan

Sodium (Na)-ion batteries (NIBs) are attracting increasing attention as next-generation energy storage systems because they do not rely on rare metals. Hard carbon (HC) is considered their most promising anode material. By tailoring the pore structure by templating methods, HC materials with a high energy density have been developed for NIBs. However, further improvements are required to achieve the desired properties without compromising the excellent characteristics already achieved. This study aims to further increase the battery capacity of zinc oxide (ZnO)–templated HC using a simple phosphorus (P)-doping method. We investigated the effects of soaking in phosphoric acid and subsequent heat treatment on the carbon morphology and electrochemical properties. The results showed that P doping increased the battery capacity without altering the ZnO–templated HC morphology. Both the sloping and plateau regions of the capacity increased, suggesting that P doping promotes Na adsorption on the carbon surface and Na storage between the layers and in the pores. Furthermore, the types of P functional groups depended on the synthesis conditions and influence the battery performance. These findings show that surface modification with specific P functional groups can effectively increase the Na storage capability of HCs.

KEYWORDS: Sodium-ion batteries, Hard carbon, Phosphorus doping, Anode, ZnO–templating

1. Introduction

The development of sustainable energy storage technologies is essential to meet the increasing global energy demand while mitigating environmental impacts. Lithium (Li)-ion batteries (LIBs) are widely used in diverse applications owing to their excellent performance, including high energy density and long cycle life [1]. However, LIBs depend on rare metals, such as Li and cobalt, as raw materials, raising concerns regarding resource shortages and price increases. Sodium (Na)-ion batteries (NIBs) are attracting attention as next-generation systems that do not require rare metals [2].

The raw materials for NIBs are abundant in the Earth's crust, and NIBs have operating principles and battery components similar to those of LIBs. However, their energy density is generally lower than that of LIBs because Na has a greater atomic mass and a higher standard electrode potential (-2.71 V versus [vs.] the standard hydrogen electrode [SHE]) than Li (-3.04 V vs. SHE). To enable practical applications, it is essential to develop electrode materials with performance comparable to those used in LIBs.

Graphite, the common anode material for LIBs, is unsuitable for NIBs owing to the instability of Na intercalation between graphene layers. While Li can be intercalated into graphite up to the composition LiC_6, the maximum Na intercalation without solvent cointercalation is limited to the composition NaC_{64} [3, 4].

Hard carbon (HC) is considered the most promising anode material for NIBs [5]. HC provides suitable Na storage sites, including enlarged interlayer spacing between graphene layers as well as numerous defects and pores. Charge–discharge profiles of half-cells with HC anodes exhibit two regions: a sloping region above 0.1 V and a plateau region below 0.1 V. Na storage mechanisms have been extensively investigated [6–18].

The "adsorption–intercalation–pore filling" model has recently

---

* Corresponding Author, E-mail: ANDO.Hideka@nims.go.jp
https://doi.org/10.7209/carbon.050106

(Received October 21, 2025, Accepted December 5, 2025)
(J-STAGE Advance published December 12, 2025)

been regarded as a plausible mechanism [7, 15, 19, 20]. This model proposes three processes: (1) adsorption at edges and defects of carbon layers in the initial sloping region, (2) intercalation into interlayer spacing from the end of the sloping region to the plateau region, and (3) pore filling toward the end of the plateau region. Additionally, Na stored in pores has been observed to form quasimetallic Na clusters near 0 V at the end of the plateau region [8, 16, 21–24]. The slope capacity supports rapid charging and discharging, whereas the plateau capacity contributes to a high energy density. Therefore, developing electrode materials tailored to specific NIB applications is necessary.

To develop carbon anode materials with increased performance, various approaches have been explored, including changing precursors, adjusting synthesis conditions, and modifying surfaces. Among these approaches, HCs synthesized using magnesium oxide (MgO)– or zinc oxide (ZnO)–templating techniques have been reported [25, 26]. These methods create numerous closed pores suitable for Na storage, particularly facilitating the formation of Na clusters that contribute to high energy density. MgO– and ZnO–templated HCs have demonstrated high capacities of 478 and 464 mAh g^{-1}, respectively, with substantial plateau capacities [25, 26]. Heteroatom doping (for example, nitrogen [N], phosphorus [P], and sulfur [S]) in HCs is another effective strategy for enhancing performance [27, 28].

P doping is particularly effective at increasing capacity [9, 29–33]. Heteroatom doping alters the morphology and physicochemical properties of HCs, including interlayer spacing, surface wettability, and electronic conductivity [34, 35]. The expansion of the interlayer spacing facilitates Na intercalation, and the introduced defects serve as Na adsorption sites. Typically, heteroatom-doped HCs are synthesized by calcining precursors containing the desired heteroatoms, such as thienyl-based polymers, N-doped carbon nanofibers, and biomass materials [36–38]. However, available heteroatom-containing precursors are limited unless specific handling procedures are employed, restricting the development of advanced materials. Another heteroatom-doping approach is the calcination of mixtures of precursors and dopants (for example, urea for N-doping, sulfur powder or sulfuric acid for S-doping, and phosphoric acid or sodium dihydrogen phosphate for P-doping) [31, 39, 40]. However, this process often impairs the inherent characteristics of undoped carbon materials. Therefore, improving the desired properties while preserving the excellent characteristics of the developed materials remains necessary.

This study proposes a simple P-doping method to increase the capacity of HCs synthesized via template methods. ZnO–templated HCs were soaked in phosphoric acid and subsequently heat-treated (220 °C and 600 °C) to introduce P dopants. Although P was presumed to be incorporated only on the surface without altering the bulk structure, slope and plateau capacities increased. Moreover, the doping conditions influenced battery performance, suggesting that the type of incorporated P is crucial in determining the electrochemical properties of HCs as NIB anode materials. This study provides novel insights into a simple P-doping method that further improves the capacity of ZnO–templated HCs without compromising the carbon morphology optimized for NIBs. The proposed method could also apply to other carbon materials for advanced NIB applications.

2. Experimental

2.1 Synthesis of ZnO–templated HC samples

ZnO–templated HC samples were prepared following a previously reported method [26]. Zinc gluconate was preheated at 600 °C at a rate of 10 °C min^{-1} and held for 1 h under N_2 gas flow (500 mL min^{-1}). The resulting product was ground using an agate mortar and sonicated in 1 M hydrochloric acid for 1 h. The material was then washed with deionized water and vacuum-dried overnight at 110 °C. The washed precursor was calcined at 1,400 °C at a rate of 10 °C min^{-1} and maintained at this temperature for 1 h under N_2 gas flow (500 mL min^{-1}). The resulting undoped ZnO–templated HC sample was designated as HC–ZnO.

P-doped HC–ZnO samples were prepared by sonicating the synthesized HC–ZnO in 1 and 2 M phosphoric acid for 1 h, followed by heat treatment. The sonicated samples were collected by vacuum filtration and heated at 220 °C overnight in air; these samples were denoted as 1M-P220 and 2M-P220, respectively. To evaluate the effect of heating temperature, the 1M-P220 sample was further heated at 600 °C for 1 h under N_2 gas flow (500 mL min^{-1}) and designated as 1M-P600.

2.2 Characterization of pristine HC samples

The morphology and elemental distribution of each sample were examined using scanning electron microscopy (SEM; TM3030Plus, Hitachi High-Tech Corp.) equipped with an energy-dispersive X-ray spectrometer (EDS). Elemental analysis of P was conducted at the Center for Organic Elemental Analysis, Kyoto University. Powder X-ray diffraction (XRD) patterns were obtained using a MiniFlex600 diffractometer (Rigaku Corp.) with copper (Cu) Kα radiation at 40 kV and 10 mA. X-ray photoelectron spectroscopy (XPS) profiles were recorded using a KRATOS AXIS-ULTRA DLD instrument (Shimadzu Corp.) with an aluminum (Al) Kα X-ray source operated at 15 kV and a 10 mA emission current.

Solid-state ^{31}P nuclear magnetic resonance (NMR) measurements were performed on an NMR system (JNM-ECZ500R, JEOL) equipped with an 11.7 T magnet at the National Institute for Materials Science. An aqueous solution of 85% phosphoric acid was used as a reference at 0 ppm. A single-pulse sequence was applied with a pulse length of 2.9 µs and a recycle delay of 30 s. The magic angle spinning (MAS) rate was 10 kHz.

2.3 Electrochemical measurements

Na half-cells were assembled using CR2032 coin cells in an argon-filled glove box. The anodes comprised HC samples as the active material, conductive carbon black (EQ-Lib-SuperP, MTI Corp.), and a poly(sodium acrylate) (Kishida Chemical Co., Ltd.) as a binder at a weight ratio of 85 : 10 : 5. Deionized water was added as the dispersion medium to form a slurry. The slurry was applied to a 100 µm thickness on Cu foil using the doctor blade method and vacuum dried at 110 °C for 1 h. After drying, the electrodes were punched to a 15.95 mm diameter and vacuum-dried overnight at 150 °C. Na metal (≧99.8%; Sigma-Aldrich Co. LLC) served as the counter electrode, and the electrolyte was 200 µL of 1.0 M $NaPF_6$ in ethylene carbonate (EC)/diethylene carbonate (DEC) (1 : 1 v/v%). A glass fiber filter (GF/D grade; Whatman) was used as the separator.

Galvanostatic charge–discharge tests (HJ1020mSD8, Hokuto Denko Corp.) were conducted to evaluate the electrochemical properties of the HC–ZnO and P-doped HC–ZnO samples. The potential range was 0.002–2.0 V (vs. Na^+/Na) at a 25 mA g^{-1} current density. During discharge, the potential was maintained at 0.002 V for 8 h. Cyclic voltammetry (CV) measurements (HZ-Pro S2A, Meiden Hokuto Corp.) were performed between 0.0 and 2.0 V (vs. Na^+/Na) at a 2 mV s^{-1} scan rate using cells after 10 galvanostatic cycles.

2.4 ^{31}P NMR measurements of sodiated and desodiated samples

The state of doped P after charge–discharge cycling was evaluated by solid-state ^{31}P MAS NMR. To eliminate P signals originating from the electrolyte, samples for NMR analysis were obtained from cells assembled with $NaClO_4$ in EC/DEC (1 : 1 v/v%) as the electrolyte rather than $NaPF_6$. Coin cells were disassembled in an argon-filled glove box after charging or discharging. The anodes were washed with dimethyl carbonate, and the anode materials were collected by scraping the electrode surface. The recovered samples were packed into NMR tubes with polyvinylidene fluoride powder to reduce conductivity effects. The experimental conditions were identical to those used for the initial HCs.

3. Results and Discussion

3.1 Characterization

The morphologies of HC–ZnO, 1M-P220, and 1M-P600 were examined using SEM. As shown in **Fig. 1**, all samples exhibited irregular particles with sizes ranging from 20 to 50 µm. P doping did not produce considerable changes in the morphology of the ZnO–templated carbon.

EDS mapping and elemental analysis of 1M-P220 and 1M-P600 are presented in **Fig. 1**(b), (c) and **Table 1**. In the EDS maps of 1M-P220, a small region with concentrated P was observed. The P concentration in the bright region was 0.81 at%, compared to 0.13 at% in the dark region (**Fig. S1** and **Table 1**). The overall P content in 1M-P220 was 0.17 at%, indicating a surface-wide P distribution. Regions of 1M-P220 with high P concentrations may contain residual phosphoric acid. In contrast, 1M-P600 showed no regions with a high P concentration.

The P content in 1M-P600, determined via EDS, decreased to 0.05 at%, likely owing to phosphoric acid pyrolysis. During heating at 400–500 °C, phosphoric acid undergoes dehydration and condensation, reacts with carbon, and is released as gaseous products [30]. Organic elemental analysis also indicated a decrease in P content from 0.25 wt% in 1M-P220 to 0.12 wt% in 1M-P600, consistent with EDS results.

The chemical states of the doped P were evaluated using XPS and ^{31}P NMR, as depicted in **Figs. 2**, **3**, respectively. The high-resolution

Table 1 EDS elemental analysis results of undoped and P-doped ZnO–template HC samples.

	Elemental Analysis/at%		
	C	O	P
HC–ZnO	96.48	3.51	—
1M-P220 (average)	94.21	5.62	0.17
1M-P220 (P accumulation area)	84.29	14.90	0.81
1M-P220 (excluding P accumulation area)	94.72	5.15	0.13
1M-P600	96.90	3.05	0.05

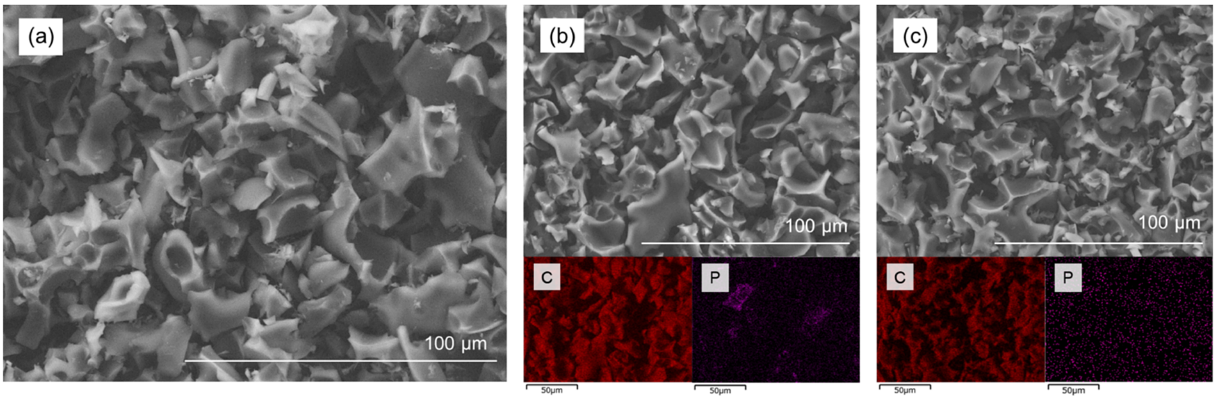

Fig. 1 (a) SEM image of HC–ZnO, (b) SEM image and EDS mapping of 1M-P220, and (c) SEM image and EDS mapping of 1M-P600.

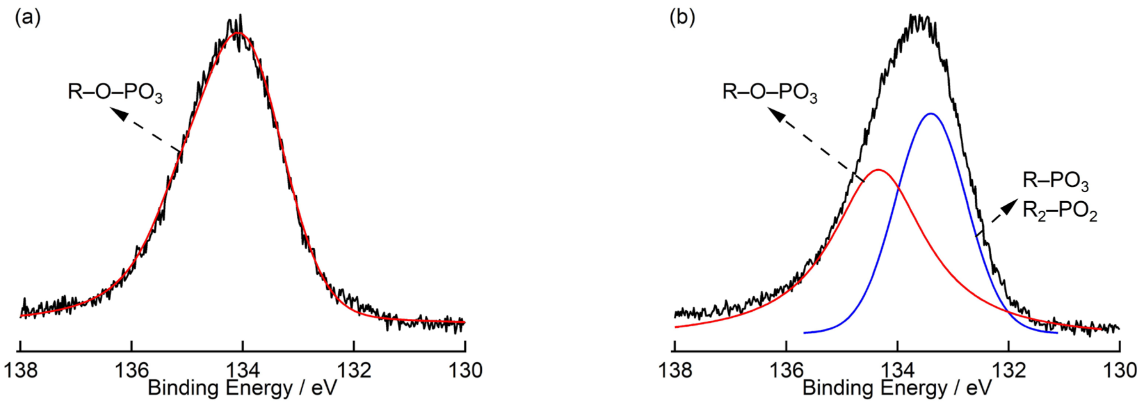

Fig. 2 High-resolution XPS profiles of the P 2p region of (a) 1M-P220 and (b) 1M-P600.

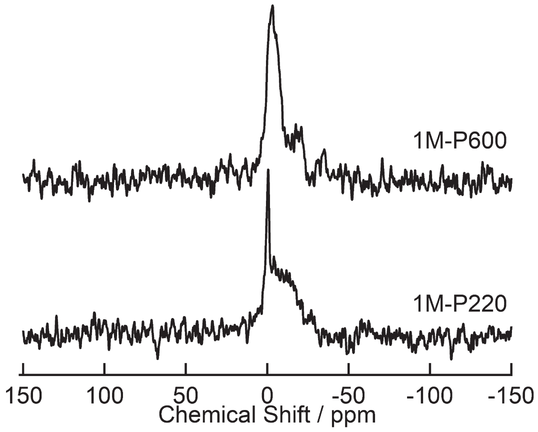

Fig. 3 ^{31}P MAS NMR spectra of pristine P-doped HC samples.

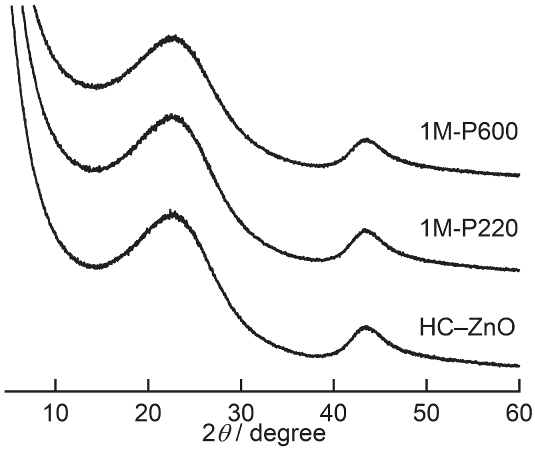

Fig. 4 XRD patterns of undoped and P-doped HC samples.

P 2p spectrum of 1M-P220 exhibited a single peak at 134.2 eV, corresponding to the phosphate groups (R–O–PO_3) [41, 42]. Additionally, the ^{31}P NMR spectra of 1M-P220 showed two types of signals: a sharp peak at 0 ppm and a broad peak at approximately −20 ppm. The sharp signal was assigned to residual phosphoric acid, consistent with EDS mapping, whereas the broad signal was attributed to R–O–PO_3 species as the chemical shift of $PO(OC_6H_5)_3$ is −18 ppm [43]. These observations align with the XPS results. The broadening of the signal reflects the structural complexity of the carbon framework bonded to phosphate species.

The XPS profile of sample 1M-P600 was deconvoluted into two peaks at 133.4 and 134.3 eV. The 134.3 eV peak corresponds to R–O–PO_3 species observed in 1M-P220, and the 133.4 eV peak was attributed to R–PO_3 and R_2–PO_2 species [44, 45]. The appearance of this additional peak indicates that high-temperature treatment promotes direct P–carbon bond formation.

The ^{31}P NMR spectrum of 1M-P600 exhibited two peaks at −4 and −18 ppm: one relatively sharp and one broad. The broad −18 ppm peak corresponds to phosphate species (R–O–PO_3), as observed in 1M-P220. The −4 ppm peak was broader and shifted to a lower frequency side than the signal at 0 ppm in 1M-P220, suggesting that it does not originate from residual phosphoric acid. Although its exact assignment remains uncertain, the correlation with XPS results suggests that this peak may originate from phosphonate functional groups containing C–P bonds. Hereinafter, this peak is referred to as the R–PO_3 species, consistent with the XPS results. These results indicate that P introduced via low-temperature treatment primarily remains as surface phosphate and residual phosphoric acid, whereas high-temperature treatment promotes direct C–P bond formation.

XRD patterns of HC–ZnO, 1M-P220, and 1M-P600 are shown in **Fig. 4**. All patterns exhibited two broad diffraction peaks at 2θ= 15–30° and 41–47°, corresponding to the 002 and 10 Bragg diffractions, respectively. Although ZnO signals were observed before acid treatment (**Fig. S2**), they disappeared in the final samples, confirming complete ZnO removal. None of the samples exhibited notable changes in peak positions or peak widths. Based on the diffraction patterns, the calculated average interlayer distance for all samples was 0.388 nm. As P doping was performed after high-temperature carbonization, no substantial structural changes were observed.

3.2 Electrochemical measurement

Galvanostatic charge–discharge testing was performed on each HC sample. In addition to ZnO–templated HCs, MgO–templated HCs were also studied following a previously reported method [25]. Although MgO–templated HCs demonstrated high capacity, consistent synthesis of samples with stable performance was sometimes challenging owing to subtle differences in the prefreezing state prior to freeze-drying and slight variations in synthesis environments. This variability prompted the selection of ZnO–templated HCs, which exhibited improved reproducibility, despite still showing some variation in reversible capacity. To evaluate the effects of P doping, the electrochemical performance of undoped and P-doped samples with the same lot numbers was compared. For clarity and traceability, each sample was labeled with its lot number appended to the sample name (for example, HC–ZnO_Lot.1). **Fig. 5**(a) presents the galvanostatic charge–discharge curves of HC–ZnO_Lot.1 and its P-doped derivatives (1M-P220_Lot.1 and 1M-P600_Lot.1). The initial charge (desodiation) capacities of HC–ZnO_Lot.1, 1M-P220_Lot.1, and 1M-P600_Lot.1 were 310, 432, and 369 mAh g^{-1}, respectively. The P-doped HC samples exhibited higher capacities than those of the undoped HC, with 1M-P220_Lot.1 showing a 39% increase. In addition, the initial coulombic efficiencies of HC–ZnO_Lot.1, 1M-P220_Lot.1, and 1M-P600_Lot.1 were 89%, 88%, and 85%, respectively. HC–ZnO_Lot.1 and 1M-P220_Lot.1 exhibited similar cycling stability during the initial five cycles (**Fig. S3**). The capacity enhancement in 1M-P220 was consistently observed across different lot numbers (**Fig. S4**). As the sample morphology remained unchanged after P doping, the improved performance is attributed to the P functional groups.

To evaluate the effect of phosphoric acid concentration on battery performance, a sample designated 2M-P220 was synthesized using 2 M phosphoric acid during doping. The initial charge capacity of 2M-P220_Lot.1 was 285 mAh g^{-1}, lower than that of HC–ZnO_Lot.1 (**Fig. S5**). HC–ZnO is likely to contain a limited number of reaction sites due to the high carbonization temperatures. Excess phosphoric acid may have remained unreacted, thereby inhibiting Na storage in HCs. Optimization of treatment conditions will be required in future studies to maximize electrochemical performance.

To analyze the changes in battery capacity, the initial charge capacities of each HC sample were separated into slope and plateau capacities at 0.1 V. The initial charge capacities of HC–ZnO_Lot.1, 1M-P220_Lot.1, and 1M-P600_Lot.1, divided into slope and plateau regions at 0.1 V, are shown in **Fig. 5**(b). The results showed that 1M-P220 exhibited a considerable increase in plateau capacity and a slight increase in slope capacity, whereas 1M-P600 showed increases in slope and plateau capacities, though to a lesser extent than 1M-P220.

Among the proposed Na storage mechanisms in HCs, slope capacity is currently considered to originate from Na adsorption on the carbon surface [7, 15, 19]. Therefore, the observed change in slope capacity upon P doping likely results from the addition of P functional groups on the carbon surface, which act as additional Na adsorption sites. Additionally, the P-doped samples exhibited increased plateau capacities.

In the plateau region, Na intercalates into the interlayer spacing of graphene layers and subsequently occupies pores near 0 V [7, 8, 15]. Thus, the observed increase in plateau capacity suggests that P doping facilitates Na storage in interlayer spacing and pores. Although P doping has been reported to alter carbon morphology and improve capacity [9, 29], in this study, the internal structure of the samples, including interlayers and pores, likely remained unaltered. It is possible that P was doped at the surfaces and entrances of carbon layers with relatively wide interlayer spacing, likely contributing to the observed capacity increase. These results indicate that surface modification is crucial in promoting Na storage within interlayer spacing and pores without directly altering the internal structure.

Another factor potentially contributing to the plateau capacity increase is enhanced pore filling. In the CV results, the cathodic peak near 0 V was not fully developed (**Fig. S6**), indicating incomplete Na storage in the pores even at 0 V [19]. HC–ZnO samples were designed with optimized pore structures for Na storage; however, some

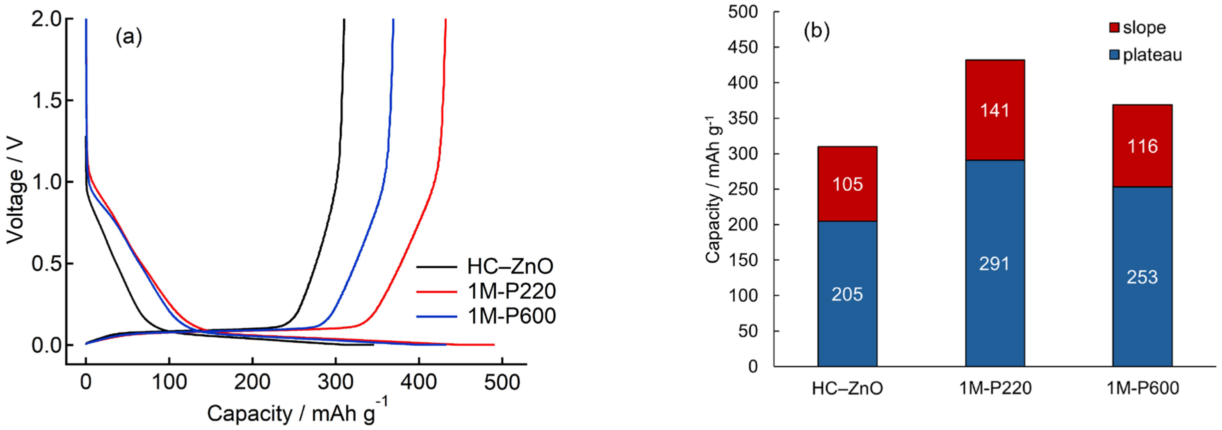

Fig. 5 (a) Initial charge–discharge profiles and (b) initial charge capacities of the slope and plateau regions for the HC–ZnO_Lot.1, 1M-P220_Lot.1, and 1M-P600_Lot.1 samples. Values within each bar indicate the corresponding capacity.

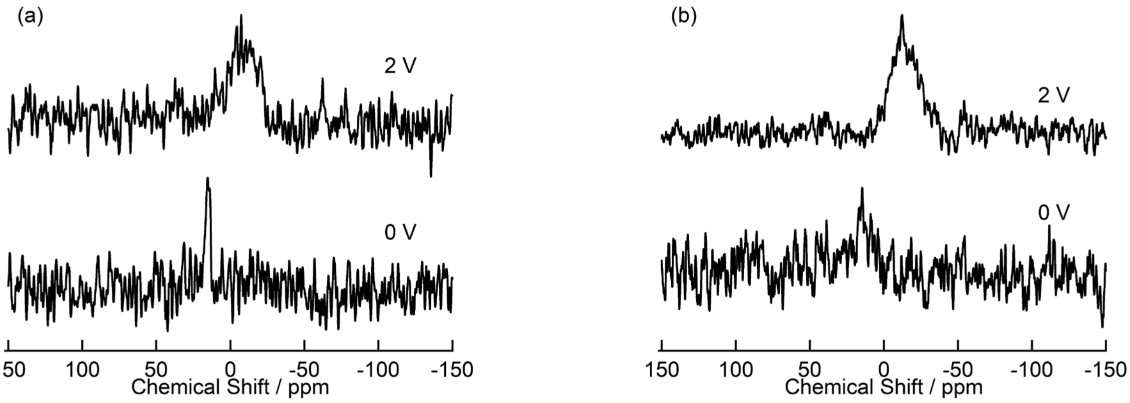

Fig. 6 ^{31}P MAS NMR spectra of (a) 1M-P220 and (b) 1M-P600 in their sodiated (bottom) and desodiated (top) states.

pores remained partially occupied. This suggests that P functional groups likely facilitated more complete pore filling rather than creating new Na storage sites. Although the specific mechanism by which P doping facilitates pore filling remains unclear, it is hypothesized that surface P functional groups reduce the energy barrier for Na access into the bulk structure.

The capacity increase owing to P doping was smaller for 1M-P600 than for 1M-P220, which was attributed to the number and types of P functional groups on the carbon surface. The P content of 1M-P600 was lower than that of 1M-P220, and XPS and ^{31}P NMR analyses identified distinct P functional groups in 1M-P220 and 1M-P600. Specifically, 1M-P220 contained only R–O–PO_3 species, whereas 1M-P600 exhibited both R–O–PO_3 and R–PO_3 species. These findings suggest that R–O–PO_3 species may be more crucial in improving battery performance than R–PO_3 species. Xie *et al.* [46] reported that PO_4 groups exhibit more favorable Na adsorption energies than pure carbon, whereas the substantially higher adsorption energy of PO_3^- groups impedes Na desorption. Additionally, they noted that C–O groups lead to irreversible capacity, whereas C=O groups enhance reversible Na adsorption. These results imply that oxygen functional groups may also be crucial in determining anodic performance. Therefore, the functional group type is likely a key factor in optimizing performance. Systematic identification and quantification of surface functional groups and their respective roles in Na storage will be addressed in future studies.

To investigate the state of doped P during charge–discharge cycling, ^{31}P NMR measurements were performed on sodiated and desodiated 1M-P220 and 1M-P600 samples. The resulting spectra are shown in **Fig. 6**. For sodiated 1M-P220, an NMR signal appeared at 15 ppm. This signal shifted to an elevated frequency and decreased in intensity relative to the signals of pristine 1M-P220. In desodiated 1M-P220, a broad signal appeared from −30 to 15 ppm, similar to the signal assigned to R–O–PO_3 species in pristine 1M-P220. These findings suggest that R–O–PO_3 species function as reversible Na storage sites. The signal corresponding to residual phosphoric acid, observed in the NMR spectra of pristine 1M-P220, disappeared after cycling, indicating its removal during the washing step prior to NMR sampling. For 1M-P600, similar signal shifts and intensity decreases were observed upon sodiation, comparable to those in 1M-P220, demonstrating that P functional groups substantially contribute to Na storage.

The observed signal shifts are likely caused by reduced electron shielding around P atoms, whereas the decreased signal intensity may result from line broadening, potentially induced by dipolar interactions with Na nuclei near P atoms. However, in desodiated 1M-P600, only a broad signal attributed to R–O–PO_3 species remained, whereas the R–PO_3 signal present in the pristine sample disappeared. This suggests that R–O–PO_3 species function as reversible Na storage sites, while R–PO_3 species are likely irreversible. The difference in functional group types may explain why the capacity of 1M-P600 is lower than that of 1M-P220.

4. Conclusion

This study investigated the effect of P doping on ZnO–templated HCs for NIB performance. P doping was performed under mild conditions by soaking HC–ZnO in phosphoric acid, followed by heating at 220 °C or 600 °C. Although the ZnO–templated HC had already been carbonized at 1,400 °C, the resulting P-doped HC samples exhibited increased battery capacities. These results demonstrate that P doping contributes to capacity enhancement without altering the carbon structure. The increased slope capacity suggests that P functional groups act as additional Na adsorption sites, while the increased plateau capacity indicates that these groups facilitate Na storage within interlayer spacing and pores. The presence of P functional groups on the carbon surface may also enhance Na accessibility to the bulk carbon matrix.

By varying the heating temperature during P doping, HC samples treated at 220 °C demonstrated greater capacity improvements than those treated at 600 °C. XPS and ^{31}P NMR analyses identified R–O–PO_3 species on the carbon surface of 1M-P220, whereas R–O–PO_3

and R–PO_3 species were detected in 1M-P600. ^{31}P NMR spectra further demonstrated strong interactions between P and Na during sodiation. Additionally, the NMR signals of R–O–PO_3 species showed high reversibility during charge–discharge cycling, whereas those of R–PO_3 species disappeared after cycling. These findings demonstrate that controlling the types of P functional groups is critical for optimizing battery performance. Overall, this study provides insights into the capacity improvement of HCs through simple P doping and supports the development of high-energy-density carbon anode materials for NIBs. This surface modification technique is not limited to P and may be extended to other heteroatom dopants introduced using different dopants, such as sulfuric and nitric acids. Systematic investigation into the effects of dopant types, base carbon structures, and treatment conditions on electrochemical performance will be a vital direction for future research.

Acknowledgements

This study was partly supported by the "Advanced Research Infrastructure for Materials and Nanotechnology in Japan (ARIM)" of the Ministry of Education, Culture, Sports, Science and Technology (MEXT), Proposal Number: JPMXP1224NM0135. Additional support was provided by JST GteX (Grant Number: JPMJGX23S4). We would like to thank Editage (www.editage.jp) for English language editing.

References

[1] Y. Nishi, The development of lithium ion secondary batteries, Chem. Rec. 1 (2001) 406–413.

[2] N. Yabuuchi, K. Kubota, M. Dahbi, S. Komaba, Research development on sodium-ion batteries, Chem. Rev. 114 (2014) 11636–11682.

[3] P. Ge, M. Fouletier, Electrochemical intercalation of sodium in graphite, Solid State Ion. 28–30 (1988) 1172–1175.

[4] K. Nobuhara, H. Nakayama, M. Nose, S. Nakanishi, H. Iba, First-principles study of alkali metal-graphite intercalation compounds, J. Power Sources 243 (2013) 585–587.

[5] X. Dou, I. Hasa, D. Saurel, C. Vaalma, L. Wu, D. Buchholz, D. Bresser, S. Komaba, S. Passerini, Hard carbons for sodium-ion batteries: Structure, analysis, sustainability, and electrochemistry, Mater. Today 23 (2019) 87–104.

[6] D.A. Stevens, J.R. Dahn, High Capacity Anode Materials for Rechargeable Sodium-Ion Batteries, J. Electrochem. Soc. 147 (2000) 1271.

[7] C. Bommier, T.W. Surta, M. Dolgos, X. Ji, New mechanistic insights on Na-ion storage in nongraphitizable carbon, Nano Lett. 15 (2015) 5888–5892.

[8] J.M. Stratford, P.K. Allan, O. Pecher, P.A. Chater, C.P. Grey, Mechanistic insights into sodium storage in hard carbon anodes using local structure probes, Chem. Commun. 52 (2016) 12430–12433.

[9] Z. Li, C. Bommier, Z.S. Chong, Z. Jian, T.W. Surta, X. Wang, Z. Xing, J.C. Neuefeind, W.F. Stickle, M. Dolgos, P.A. Greaney, X. Ji, Mechanism of Na-ion storage in hard carbon anodes revealed by heteroatom doping, Adv. Energy Mater. 7 (2017) 1602894.

[10] S. Qiu, L. Xiao, M.L. Sushko, K.S. Han, Y. Shao, M. Yan, X. Liang, L. Mai, J. Feng, Y. Cao, X. Ai, H. Yang, J. Liu, Manipulating adsorption–insertion mechanisms in nanostructured carbon materials for high-efficiency sodium ion storage, Adv. Energy Mater. 7 (2017) 1700403.

[11] H. Lu, F. Ai, Y. Jia, C. Tang, X. Zhang, Y. Huang, H. Yang, Y. Cao, Exploring sodium-ion storage mechanism in hard carbons with different microstructure prepared by ball-milling method, Small 14 (2018) e1802694.

[12] P. Bai, Y. He, X. Zou, X. Zhao, P. Xiong, Y. Xu, Elucidation of the sodium-storage mechanism in hard carbons, Adv. Energy Mater. 8 (2018) 1703217.

[13] S. Alvin, D. Yoon, C. Chandra, H.S. Cahyadi, J.-H. Park, W. Chang, K.Y. Chung, J. Kim, Revealing sodium ion storage mechanism in hard carbon, Carbon 145 (2019) 67–81.

[14] N. Sun, Z. Guan, Y. Liu, Y. Cao, Q. Zhu, H. Liu, Z. Wang, P. Zhang, B. Xu, Extended "adsorption–insertion" model: A new insight into the sodium storage mechanism of hard carbons, Adv. Energy Mater. 9 (2019) 1901351.

[15] Y. Morikawa, S. Nishimura, R. Hashimoto, M. Ohnuma, A. Yamada, Mechanism of sodium storage in hard carbon: An X-ray scattering analysis, Adv. Energy Mater. 10 (2020) 1903176.

[16] H. Au, H. Alptekin, A.C.S. Jensen, E. Olsson, C.A. O'Keefe, T. Smith, M. Crespo-Ribadeneyra, T.F. Headen, C.P. Grey, Q. Cai, A.J. Drew, M.-M. Titirici, A revised mechanistic model for sodium insertion in hard carbons, Energy Environ. Sci. 13 (2020) 3469–3479.

[17] J. Han, I. Johnson, Z. Lu, A. Kudo, M. Chen, Effect of local atomic structure on sodium ion storage in hard amorphous carbon, Nano Lett. 21 (2021) 6504–6510.

[18] L. Kitsu Iglesias, E.N. Antonio, T.D. Martinez, L. Zhang, Z. Zhuo, S.J. Weigand, J. Guo, M.F. Toney, Revealing the sodium storage mechanisms in hard carbon pores, Adv. Energy Mater. 13 (2023) 2302171.

[19] X. Chen, J. Tian, P. Li, Y. Fang, Y. Fang, X. Liang, J. Feng, J. Dong, X. Ai, H. Yang, Y. Cao, An overall understanding of sodium storage behaviors in hard carbons by an "adsorption–intercalation/filling" hybrid mechanism, Adv. Energy Mater. 12 (2022) 2200886.

[20] J. Zhao, X.-X. He, W.-H. Lai, Z. Yang, X.-H. Liu, L. Li, Y. Qiao, Y. Xiao, L. Li, X. Wu, S.-L. Chou, Catalytic defect-repairing using manganese ions for hard carbon anode with high-capacity and high-initial-coulombic-efficiency in sodium-ion batteries, Adv. Energy Mater. 13 (2023) 2300444.

[21] R. Morita, K. Gotoh, K. Kubota, S. Komaba, K. Hashi, T. Shimizu, H. Ishida, Correlation of carbonization condition with metallic property of sodium clusters formed in hard carbon studied using ^{23}Na nuclear magnetic resonance, Carbon 145 (2019) 712–715.

[22] K. Gotoh, T. Yamakami, I. Nishimura, H. Kometani, H. Ando, K. Hashi, T. Shimizu, H. Ishida, Mechanisms for overcharging of carbon electrodes in lithium-ion/sodium-ion batteries analysed by operando solid-state NMR, J. Mater. Chem. A 8 (2020) 14472–14481.

[23] A. Rajh, M. Gabrijelčič, B. Tratnik, K. Bučar, I. Arčon, M. Petric, R. Dominko, A. Vizintin, M. Kavčič, Structural and chemical analysis of hard carbon negative electrode for Na-ion battery with X-ray Raman scattering and solid-state NMR spectroscopy, Carbon 228 (2024) 119398.

[24] M. Gabrijelčič, B. Tratnik, G. Kapun, E. Tchernychova, N. Zabukovec Logar, A. Krajnc, R. Dominko, A. Vizintin, Probing sodium structures and dynamics in hard carbon for Na-ion batteries using ^{23}Na operando solid-state NMR spectroscopy, J. Mater. Chem. A 13 (2025) 1042–1056.

[25] A. Kamiyama, K. Kubota, D. Igarashi, Y. Youn, Y. Tateyama, H. Ando, K. Gotoh, S. Komaba, MgO-template synthesis of extremely high capacity hard carbon for Na-ion battery, Angew. Chem. Int. Ed. 60 (2021) 5114–5120.

[26] D. Igarashi, Y. Tanaka, K. Kubota, R. Tatara, H. Maejima, T. Hosaka, S. Komaba, New template synthesis of anomalously large capacity hard carbon for Na- and K-ion batteries, Adv. Energy Mater. 13 (2023) 2302647.

[27] W. Chen, M. Wan, Q. Liu, X. Xiong, F. Yu, Y. Huang, Heteroatom-doped carbon materials: Synthesis, mechanism, and application for sodium-ion batteries, Small Methods 3 (2019) 1800323.

[28] Y. Li, M. Chen, B. Liu, Y. Zhang, X. Liang, X. Xia, Heteroatom doping: An effective way to boost sodium ion storage, Adv. Energy Mater. 10 (2020) 2000927.

[29] Z. Li, L. Ma, T.W. Surta, C. Bommier, Z. Jian, Z. Xing, W.F. Stickle, M. Dolgos, K. Amine, J. Lu, T. Wu, X. Ji, High capacity of hard carbon anode in Na-ion batteries unlocked by POx doping, ACS Energy Lett. 1 (2016) 395–401.

[30] Y. Li, Y. Yuan, Y. Bai, Y. Liu, Z. Wang, L. Li, F. Wu, K. Amine, C. Wu, J. Lu, Insights into the Na^+ storage mechanism of phosphorus-functionalized hard carbon as ultrahigh capacity anodes, Adv. Energy Mater. 8 (2018) 1702781.

[31] S. Alvin, C. Chandra, J. Kim, Extended plateau capacity of phosphorus-doped hard carbon used as an anode in Na- and K-ion batteries, Chem. Eng. J. 391 (2020) 123576.

[32] H. Ando, K. Hashi, S. Ohki, Y. Hatakeyama, Y. Nishina, N. Kowata, T. Ohkubo, K. Gotoh, State change of Na clusters in hard carbon electrodes and increased capacity for Na-ion batteries achieved by heteroatom doping, Carbon Trends 16 (2024) 100387.

[33] X. Wang, J. Dong, J. Ren, K. Wang, X. Li, J. Li, J. Tao, Phosphorus-doped coal-derived hard carbon anodes for high-performance sodium-ion batteries: Synergistic regulation of graphitization and sodium adsorption, Electrochim. Acta 536 (2025) 146731.

[34] Q. Lin, J. Zhang, W. Lv, J. Ma, Y. He, F. Kang, Q.-H. Yang, A functionalized carbon surface for high-performance sodium-ion storage, Small 16 (2020) e1902603.

[35] H. Zhang, S. Lin, C. Shu, Z. Tang, X. Wang, Y. Wu, W. Tang, Advances and perspectives of hard carbon anode modulated by defect/hetero elemental engineering for sodium ion batteries, Mater. Today 85 (2025) 231–252.

[36] J.P. Paraknowitsch, A. Thomas, J. Schmidt, Microporous sulfur-doped carbon from thienyl-based polymer network precursors, Chem. Commun. 47 (2011) 8283–8285.

[37] J. Zhu, C. Chen, Y. Lu, Y. Ge, H. Jiang, K. Fu, X. Zhang, Nitrogen-doped carbon nanofibers derived from polyacrylonitrile for use as anode material in sodium-ion batteries, Carbon 94 (2015) 189–195.

[38] G. Xu, J. Han, B. Ding, P. Nie, J. Pan, H. Dou, H. Li, X. Zhang, Biomass-derived porous carbon materials with sulfur and nitrogen dual-doping for energy storage, Green Chem. 17 (2015) 1668–1674.

[39] W. Li, M. Zhou, H. Li, K. Wang, S. Cheng, K. Jiang, A high performance sulfur-doped disordered carbon anode for sodium ion batteries, Energy Environ. Sci. 8 (2015) 2916–2921.

[40] H. Hou, L. Shao, Y. Zhang, G. Zou, J. Chen, X. Ji, Large-area carbon nanosheets doped with phosphorus: A high-performance anode material for sodium-ion batteries, Adv. Sci. 4 (2017) 1600243.

[41] J. Bedia, J.M. Rosas, J. Márquez, J. Rodríguez-Mirasol, T. Cordero, Preparation and characterization of carbon based acid catalysts for the dehydration of 2-propanol, Carbon 47 (2009) 286–294.

[42] G. Hasegawa, T. Deguchi, K. Kanamori, Y. Kobayashi, H. Kageyama, T. Abe, K. Nakanishi, High-level doping of nitrogen, phosphorus, and sulfur into activated carbon monoliths and their electrochemical capacitances, Chem. Mater. 27 (2015) 4703–4712.

[43] M. Hesse, H. Meier, B. Zeeh, Spectroscopic methods in organic chemistry, 2nd ed., Thieme, Stuttgart, 2008.

[44] L. Wang, X. Dong, H. Jiang, G. Li, M. Zhang, Phosphorylated ordered mesoporous carbon as a novel solid acid catalyst for the esterification of oleic acid, Catal. Commun. 56 (2014) 164–167.

[45] X. Yan, Y. Liu, X. Fan, X. Jia, Y. Yu, X. Yang, Nitrogen/phosphorus co-doped nonporous carbon nanofibers for high-performance supercapacitors, J. Power Sources 248 (2014) 745–751.

[46] F. Xie, Y. Niu, Q. Zhang, Z. Guo, Z. Hu, Q. Zhou, Z. Xu, Y. Li, R. Yan, Y. Lu, M.-M. Titirici, Y.-S. Hu, Screening heteroatom configurations for reversible sloping capacity promises high-power Na-ion batteries, Angew. Chem. Int. Ed. 61 (2022) e202116394.